HIGH-GROWTH-FACTOR IMPLOSIONS (HEP4)

O. L. Landen
C. J. Keane
B. A. Hammel
W. K. Levedahl
R. E. Chrien*
N. D. Hoffman*
J. D. Colvin*
P. A. Amendt
S. P. Hatchett
M. M. Marinak
L. J. Suter
M. D. Cable
R. Cook
T. R. Dittrich
S. W. Haan
R. G. Hay
R. J. Wallace
H. N. Kornblum
R. A. Lerche
R. L. McEachern
T. J. Murphy
M. B. Nelson

Introduction

In inertial confinement fusion (ICF),[1,2] the kinetic energy of an ablating, inward-driven, solid spherical shell is used to compressionally heat the low-density fuel inside. For a given drive, the maximum achievable compressed fuel density and temperature—and hence the maximum neutron production rate—depend on the degree of shell isentropy[2,3] and integrity maintained during the compression. Shell integrity will be degraded by hydrodynamic instability growth[2,4–7] of areal density imperfections in the capsule. Surface imperfections on the shell grow as a result of the Richtmyer–Meshkov[8] and Rayleigh–Taylor[9] (RT) instabilities when the shell is accelerated by the ablating lower-density plasma. Perturbations at the outer capsule surface are transferred hydrodynamically to the inner surface, where deceleration of the shell by the lower-density fuel gives rise to further RT growth at the pusher–fuel interface. A widely used dispersion relation[5,10] for the RT growth rate γ in the presence of a density scalelength L and a mass ablation rate dm/dt is

$$\gamma = \left[\frac{kg}{(1+kL)}\right]^{1/2} - \frac{\beta k}{\rho}\frac{dm}{dt}\,, \qquad (1)$$

where k is the wave number of the seeding perturbation, g is the acceleration or deceleration, β is a constant between 1 and 3 determined empirically, and ρ is the peak shell density. Equation (1) indicates that γ increases as interfaces become sharper (smaller L), as peak shell densities increase, and as mass ablation rates decrease.

Implosion Design

In the HEP3 implosion campaign,[6] the unsaturated to weakly nonlinear low-growth regime was studied. See the previous article, "Diagnosis of Pusher–Fuel Mix in Indirectly Driven Nova Implosions (HEP3)," p. 265 for a discussion. Unshaped drive pulses and low-opacity plastic capsules were used, which allowed strong shock and hard x-ray preheating. This led to shallower ablation-front gradients and lower shell densities during the implosion phase. The goal of the HEP4 campaign was to increase susceptibility to RT growth in a more isentropic implosion. HEP4 designs[11] have used shaped drive, and x-ray preheat shielding,[12] by adding mid-Z dopants in the capsule ablator for reducing preheat.

Role of Doped Ablators

Use of a mid-Z dopant in the ablator has three principal effects. First, these dopants are chosen to preferentially absorb the 1–3-keV x rays (arising from the Au hohlraum laser plasmas) that volumetrically preheat Nova-scale plastic shells most efficiently. A cooler shell will expand less quickly, thereby maintaining a higher shell density ρ and steeper interface density gradients for a longer time.[13] Second, doping reduces the ablation scalelength by reducing the distance over which the soft drive x rays[14] are absorbed. Third, the increase in shell density leads to a thinner shell during compression and thus gives rise to more efficient feedthrough of surface perturbations with skin depths $\approx 1/k$. These effects combine to increase predicted maximum linear growth factors GF (ratios of final pusher–fuel to initial outside surface perturbation amplitudes) from 10 to 110 as the doping is increased from 0 with no pulse shaping (HEP3 conditions)[6] to 2 at.% Ge or Br with a two-step pulse (HEP4 conditions).[13] Mid-Z dopants, in particular Br, were used extensively to increase growth factors[15] in planar RT experiments[16] conducted in the HEP2 campaign.

---

* Los Alamos National Laboratory, Los Alamos, New Mexico

A linear GF of 100, for example means that, in the absence of saturation, an initial perturbation amplitude of 0.1 µm with mode number $l = kr(t)$ on the surface of a capsule of radius r would lead to a 10-µm perturbation of the same mode number at the pusher–fuel interface at peak neutron production time. In general, a full spectrum of randomly phased modes will initially be present. Each mode number will have a different predicted GF through the dependence on wave number k in Eq. (1). Growth of high-mode-number perturbations (large k) is reduced by ablation, density gradients, inefficient feedthrough, and (when amplitudes become comparable to the wavelength) by the onset of saturation. Long wavelengths (small k) have low growth rates from the outset. One can therefore expect a bell-shaped growth factor spectrum that peaks near some intermediate mode number.[13]

Instability Growth Modeling

Until recently, three-dimensional (3-D) codes handling multimode growth up to and beyond saturation have not been available or practicable. In their place, a multimode mix model[4,6] has been used extensively, as described more fully in “Diagnosis of Pusher–Fuel Mix in Indirectly Driven Nova Implosions (HEP3)” on p. 265 of this *Quarterly*. Briefly, a series of linear single-mode growth-rate simulations is used to calculate the amplitude evolution of each mode initially present on the capsule surface, starting with amplitudes small enough to ensure that the growth remains linear throughout the implosion. The time dependence of the linear mode amplitudes are then obtained by multiplying these growth factors by the initial amplitude spectrum. If the individual amplitudes grow large enough ($\geq 2r/l^2$), they are corrected for saturation in the presence of a full spectrum of modes.[4] The quadrature sum of the perturbation amplitudes fed through to the pusher–fuel interface is then used to set the annular width for a one-dimensional (1-D) model of atomically mixed shell and fuel located at the shell–fuel interface. A 1-D implosion simulation incorporating this evolving mix layer is then used to predict observables such as neutron yield. The yield drops as the calculated mix width becomes a larger fraction of the converged fuel radius, principally because of enhanced conduction cooling by shell material penetrating closer to the central, hottest fuel region, which provides most of the fusion reactions.

Figure 1 shows the calculated mix amplitudes (normalized to converged fuel radius at peak neutron emission time and defined as approximately one-third the mix width) vs initial outside surface roughness for the low-growth HEP3 implosions, the present HEP4 implosions, and the proposed National Ignition Facility (NIF) conditions.[17] The gray lines with unit slope correspond to assuming no growth saturation. The departure from unit slope for each black curve signifies the predicted onset of growth saturation. A typical intrinsic surface roughness power spectrum was assumed for these calculations. The large fractional mix widths calculated for the NIF implosions are a consequence of the more elaborate pulse shaping used to keep NIF implosions nearly isentropic. Ignition for NIF will require that the final mix amplitude not exceed about one-fifth of the converged capsule radius.[17] This criterion is equivalent to a factor of ~2 yield reduction for nonigniting target designs such as those used in HEP3 and HEP4. The present HEP4 experiments were designed to span both sides of this threshold by varying initial surface roughnesses from 0.01 µm rms upward, while approaching the growth factors expected of the NIF targets.

Figure 1 shows that a necessary condition for ignition sets the upper limit on initial capsule outside surface finish at a currently achievable roughness of 0.03 µm rms. If there were no growth saturation, NIF capsules would need to be considerably smoother (by a factor of 2), which is at the limit of current technology. A specific goal of the HEP4 campaign was therefore to test the validity of the growth saturation model.

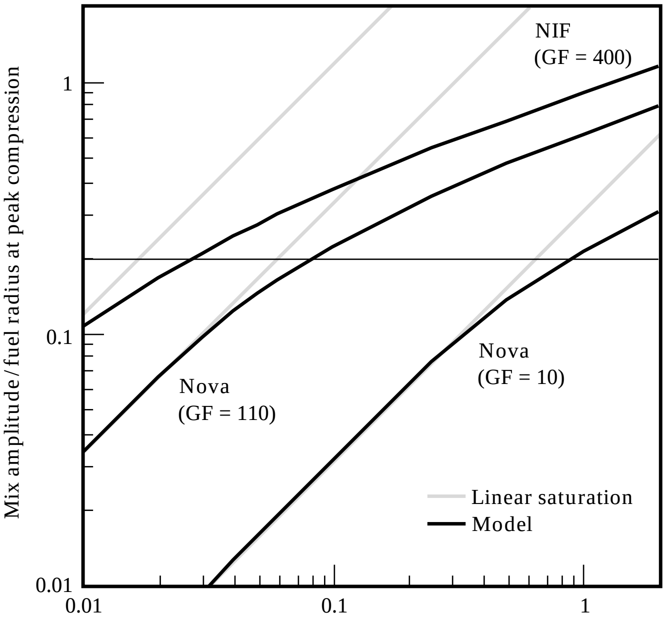

FIGURE 1. Calculated mix amplitude (normalized to fuel radius at peak neutron emission time) vs initial surface roughness. Starting from the right, the three curves correspond to the low-growth HEP3 design, the present higher-growth HEP4 design, and the NIF design. Black and gray curves correspond to calculations with and without growth saturation, respectively. The section of the NIF curve above a normalized mix amplitude of 0.2 corresponds to loss of ignition. (20-03-0995-2096pb01)

Capsule Design

Figure 2 shows the cross section of a typical capsule. The ablator, a 1.1–1.3 g / cm^3 plasma-polymerized plastic ($CH_{1.3}$), typically 39 µm thick, is doped[18] with up to 3 at.% Br or Ge. The early experiments used Br doping; the later experiments switched to Ge, which was more robust and easier to fabricate. A 3-µm polyvinyl alcohol (PVA) intermediate layer serves to confine the fuel. In early experiments, the inner polystyrene shell (~440 µm i.d. and 3 µm thick) was doped with 0.07 at.% Ti. The fuel consists of 25 atm each of D_2 and H_2, doped with 0.05 at.% Ar. The dilution of the D with H was necessary to avoid saturation in the secondary-neutron detector. The Ar and Ti serve as noninvasive emission diagnostics of electron temperature and electron density and of the spatial profile of the fuel and shell during the burn phase. Figure 3 shows the initial shell optical depth vs photon energy and shows, for example, that 1.3 at.% Ge doubles the initial capsule optical depth above the Ge ($n = 2$) bound–free absorption edge at 1.2 keV. Simulations using the measured photon flux above 1.2 keV indicate that such shielding reduces the entropy of the inner shell surface relative to the undoped case by 20% before the first shock arrives at 1 ns.

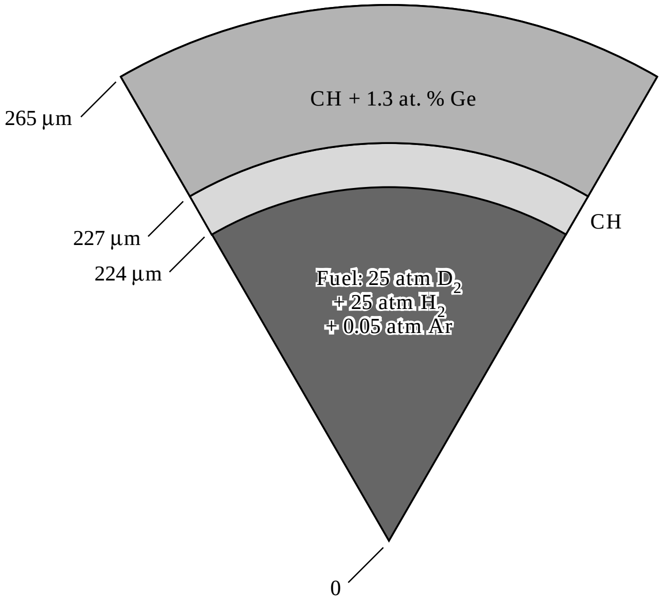

FIGURE 2. Cross section of a typical deuterated-fuel capsule design. (20-03-0995-2107pb03)

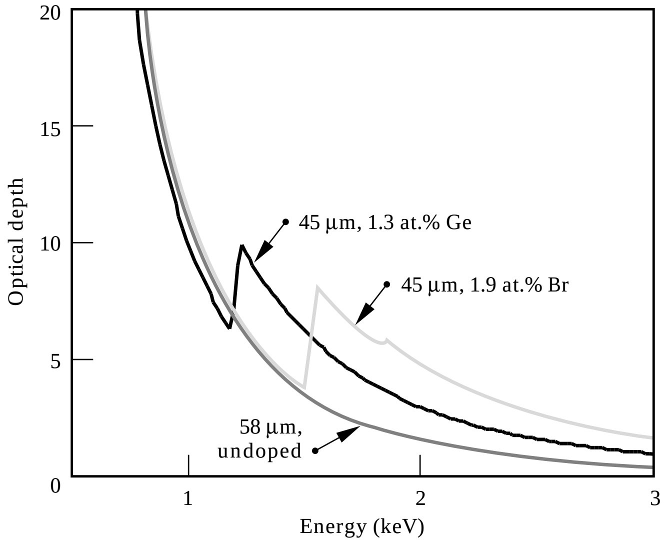

FIGURE 3. Initial capsule ablator opacity vs photon energy for 58-µm-thick undoped plastic ablators and for 45-µm-thick 1.3 at.% Ge and 1.9 at.% Br-doped plastic ablators. (20-03-0995-2099pb01)

The RT seeding is provided by pre-roughening the capsule surface by ultraviolet (UV) laser ablation[19] of 200 randomly distributed 75-µm-diam pits of equal depths, which yields a continuous distribution of perturbation wave numbers. The surface roughness is quantified by averaging a series of circumferential depth profiles obtained by atomic force microscopy.[20] The profiles are Fourier-transformed to yield 1-D power spectra, which are found to be in excellent agreement with spectra predicted by a model assuming randomly located pits of the measured shape. By assuming isotropy, 1-D spectra can be converted[21] to 2-D power spectra, which serve as input to simulations. A simple measure of the surface roughness is taken to be the square root of the summed power spectra, expressed as a rms roughness. For the purposes of defining roughness, the lowest order modes ($l < 10$), which grow the least according to Eq. (1), are not included. By varying the pit depths, rms roughnesses so defined covered the range between 0.01 and 2 µm.

Hohlraum Drive

The capsules are mounted in the center of a 2400-µm-long, 1600-µm-diam Au hohlraum with 1200-µm-diam laser entrance holes on each end. A hohlraum of pentagonal cross section was used to avoid line focusing of reflected laser light onto the capsule surface, as is observed with cylindrical hohlraums. X-ray and optical measurements indicate that such line foci reach irradiances of 10^{14} W / cm^2 over the first 200 ps, which could seed RT-unstable perturbations of similar magnitude to some of the smaller amplitude ablated pits.

The soft x-ray drive was generated by irradiating the inner hohlraum walls with ten accurately synchronized (10 ps rms fluctuation), precision-pointed (30 µm rms fluctuation), power-balanced (<10% rms fluctuation),[22] 0.35-µm, 2.2-ns-long, 3-kJ Nova pulses. Figure 4(a) shows the absorbed power from a ramped pulse shape, called PS26, chosen to provide reduced shock preheating[23] and to more closely approximate ignition-scale drive. The average x-ray flux at the capsule, plotted in Fig. 4(a) as a blackbody flux temperature, was inferred from filtered, time-resolved, multichannel (Dante) measurements[24] of x-ray re-emission from the hohlraum walls. Measurements were performed on both laser-irradiated and unirradiated walls.[25] The drive was independently inferred from simultaneous UV shock breakout measurements[26] using Al wedges [Fig. 4(b)]; the results are in good agreement with simulations based on the measured drive shown in Fig. 4(a). The peak drive temperature was 237 ± 7 eV; the uncertainty corresponds to a factor of 2 uncertainty in calculated neutron yield.

Harder x rays emanating from the high-temperature, low-density Au laser plasmas (principally Au $n = 4$ to $n = 3$ and $n = 5$ to $n = 3$ transitions between 2 and 4 keV) are also present. Figure 3 shows that the ablator optical depth is only 1 to 2 for these x rays, making them an important source of preheating of the inner shell. Their fractional contribution to the total drive at the capsule (shown in Fig. 5) was determined from a solid-angle average formed by combining the Dante localized absolute flux measurements with 2-D spatially resolved x-ray images of the hohlraum wall. We attribute the initial spike in the hard x-ray fraction to reflected laser light efficiently illuminating much of the hohlraum walls; 0.1 ns later, plasma expansion has greatly diminished the reflectivity and localized the hard x-ray production at the first-hit locations of the laser. The error bars represent only Dante uncertainties; the assumption of an optically thick Lambertian source for the harder x rays may result in an additional 2× underestimate of their fraction. However, simulations show that admitting a total factor of 3 underestimate in hard x-ray fraction will decrease yields for 1.3 at.% Ge-doped capsules by only 30%.

Deuterated Fuel Capsules

The implosions are diagnosed by primary and secondary neutron yields,[27] neutron production times,[28] time-resolved x-ray imaging,[29] and time-resolved x-ray spectroscopy of tracer dopants in the shell and fuel.[13,23,30,31] The results of an early campaign with Br-doped capsules have been published elsewhere.[30] The newer Ge-doped capsule implosion results described here have been more thoroughly characterized and modeled. Results are compared with predictions made using the 2-D radiation hydrodynamics code LASNEX.[32] A new 3-D radiation hydrodynamics code, HYDRA,[33] is also being used to simulate these high-growth-factor implosions.

Performance vs Preheat Shielding

The first HEP4 implosions served to test our understanding of the behavior of the smoothest available plastic capsules as ablator doping was increased. In the limit of negligible RT growth, one would expect that the increase in in-flight shell density ρ due to preheat shielding provided by the mid-Z dopant would improve capsule performance. Specifically, for a fixed implosion velocity v, the compressional pressure[2,3,10] ρv^2 that determines the final fuel areal density and yield achievable should increase with ρ.

Figure 6 shows that the measured yield does indeed increase with Ge doping, with a slope consistent with that of the corresponding 1-D simulations. Peak neutron production times (2.2 ± 0.1 ns) and hence implosion velocities were kept fixed by varying the initial ablator thicknesses (from 44 µm at 2 at.% Ge to 58 µm for undoped ablators) to compensate for changes in initial shell density and opacity when incorporating Ge in the ablator. Capsules were selected for best surface finish

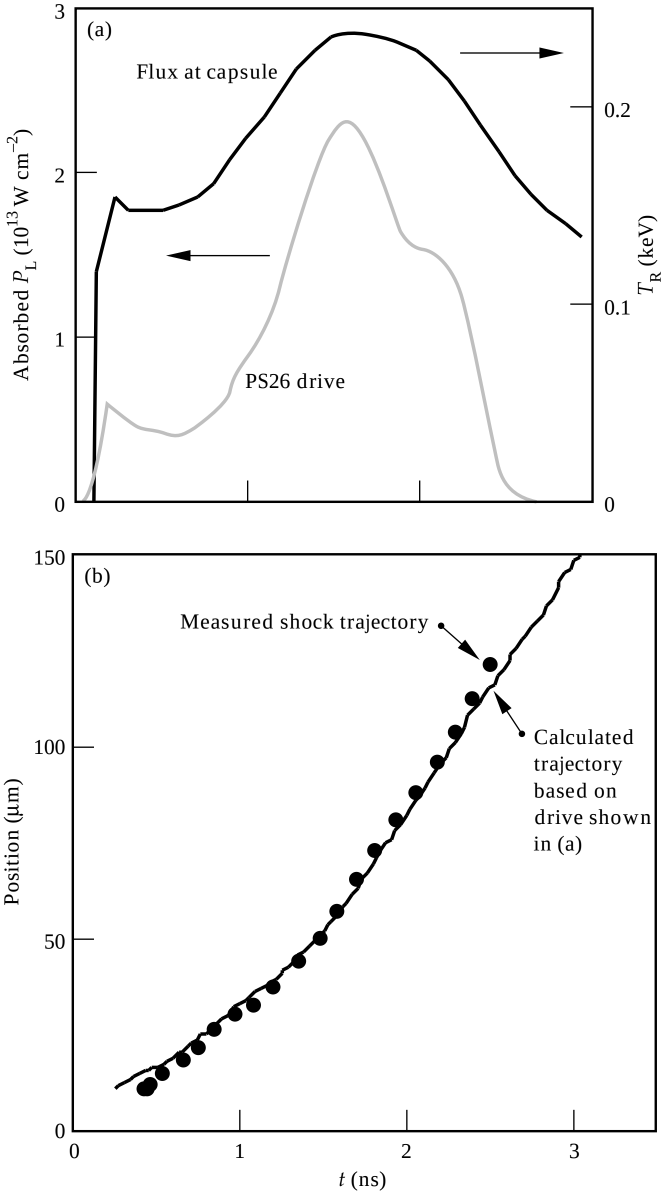

FIGURE 4. (a) Measured absorbed laser power and measured soft x-ray flux (plotted as a blackbody flux temperature) from absolutely calibrated filtered diode array (Dante). (b) Measured shock trajectory in Al wedge and corresponding predicted trajectory based on the x-ray drive in (a). (20-03-0995-2100pb01)

(<0.03 μm rms roughness). The simulations used the measured drive flux and spectrum at each time as baseline input, with slight modifications for (<10%) shot-to-shot variations in laser energy and capsule dimensions. The systematic factor of 3–4 discrepancy between simulated and measured yields for smooth capsules is not completely understood, but 3-D calculations which include long wavelength shell thickness variations significantly reduce this discrepancy. These calculations are described in the section "Recent Modeling Advances." Nevertheless, the increase in yield as preheat shielding is increased for best surface finish capsules is encouraging for NIF, because it demonstrates a hydrodynamically similar implosion for which the beneficial effects of a more isentropic compression outweigh the detrimental effects of increased susceptibility to RT growth.

Figure 7 displays 4-keV x-ray snapshots showing a reduction in imploded core image size as the ablator doping is increased from zero to 1.3 to 2.7 at.% Ge. The core images, captured with 7-μm and 80-ps resolution by gated pinhole cameras, are dominated by Ar bound–free emission from the doped fuel. Figure 7(d) shows the azimuthally averaged 50% contour diameters extracted from such images. The average measured x-ray radii decrease monotonically with increasing Ge doping, with a slope consistent with post-processed 2-D integrated hohlraum and capsule simulations of image size, but with an overall 30% size reduction.

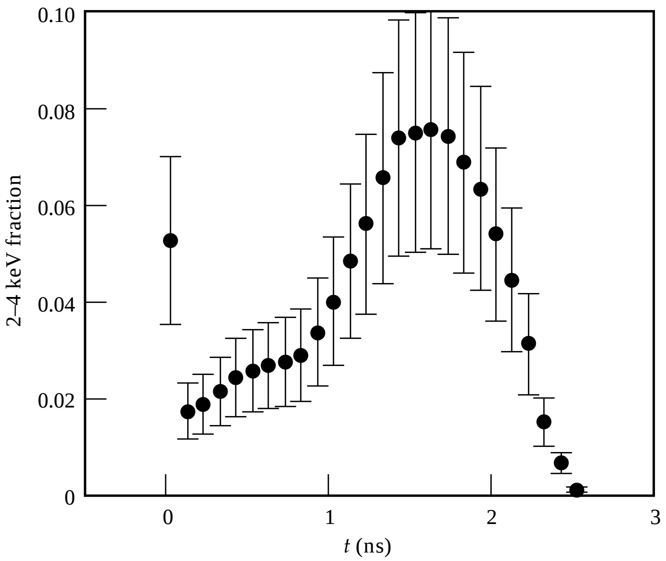

FIGURE 5. Measured 2–4-keV hohlraum power as a fraction of total x-ray power. Error bars represent uncertainty in Dante calibration and unfold only. (20-03-0995-2101pb01)

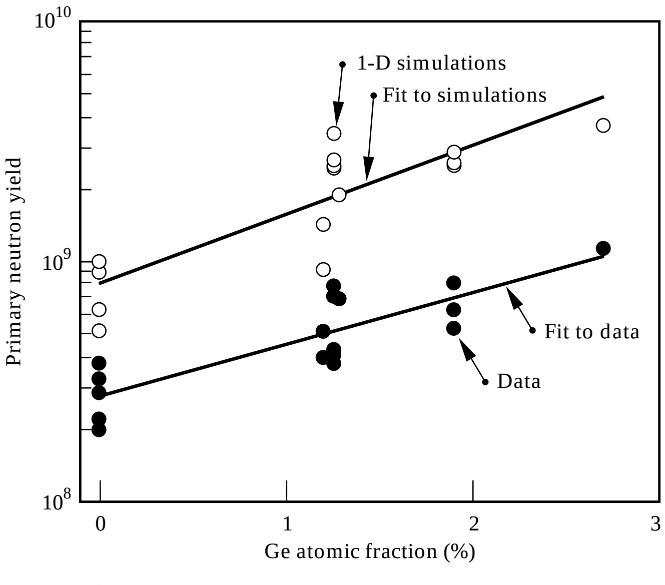

FIGURE 6. Measured and calculated primary (DD) neutron yields vs doping for smooth capsules. Solid lines are linear fits to data and simulations. (20-03-0995-2103pb01)

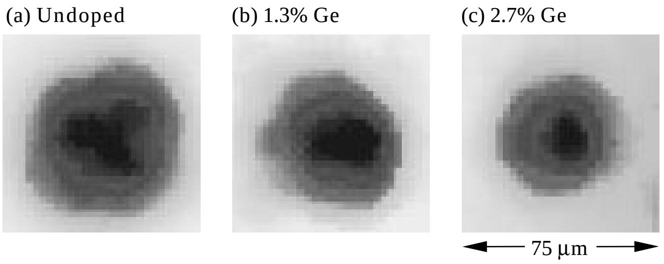

(d) FWHM vs Ge atomic fraction

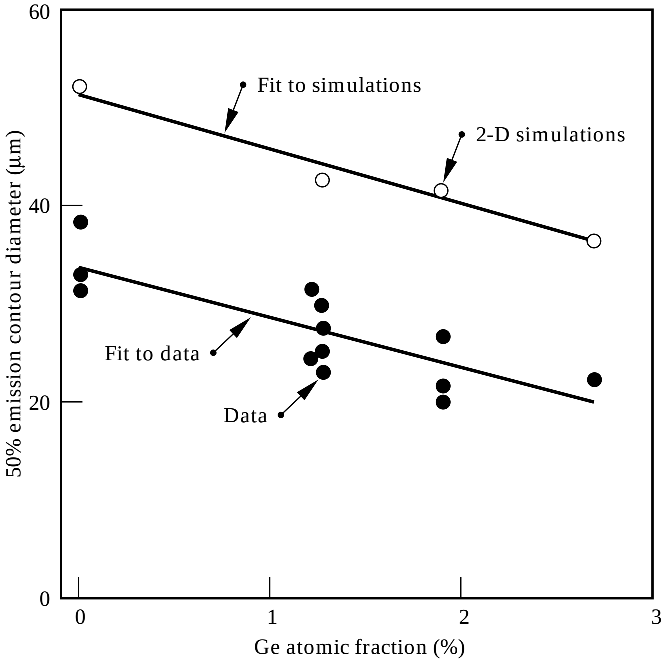

FIGURE 7. X-ray images at 4 keV of imploded cores from smooth capsules at peak emission time for (a) no doping, (b) 1.3 at.% Ge, and (c) 2.7 at.% Ge. (d) Measured (solid circles) and calculated (open circles) azimuthally averaged diameters of 50% x-ray emission contours vs Ge doping. Solid lines are linear fits to data and simulations. (20-03-0995-2102pb01)

Fuel areal densities and (by invoking particle conservation) fuel convergences were also inferred from the fraction of secondary DT reactions and the resultant secondary-neutron energy spectrum[27] measured by a large neutron scintillator array (LaNSA). This diagnostic technique, used extensively in the HEP1 campaign,[25] works on the principle that the triton produced in the primary DD reaction undergoes secondary DT reactions with a probability that depends on the areal density of deuterons seen by the escaping triton. At all Ge dopings, the inferred fuel convergences are within 10% of the values obtained from simulations. To reconcile the x-ray size discrepancy with the agreement in convergence, we note that emissivities for kilovolt x-ray photons are sensitive to sub-kilovolt variations in plasma temperature, while the secondary reaction between MeV tritons and deuterons is not. Hence the 30% overprediction in x-ray core image size shown in Fig. 7(d) may be evidence that the simulations, while correctly predicting the final fuel radius, overpredict the plasma temperature in the outer regions of the compressed fuel. Such increased cooling is seen in 3-D calculations which include long wavelength variations in capsule wall thickness.

Spatially integrated, time-resolved spectra of Ar and Ti line and continuum emission were also recorded during the fusion phase.[30] The emission lines of interest are those of He-like Ti (1s2p–1s^2) and of optically thin He-like Ar (1s3p–1s^2) and H-like Ar (3p–1s). The measured Ar and Ti line durations for 1.9 at.% Br-doped capsules were 150 and 80 ps FWHM, respectively, half the corresponding durations for undoped capsules and in good agreement with simulations. Predicted H-like emission from the Ti dopant in the inner portion of the shell was not observed, again suggesting that the volume comprising the outer regions of the fuel and the inside of the shell is cooler than expected.

The agreement between measured and predicted trends in capsule performance as preheat shielding is increased indicates that the goal of mimicking more isentropic NIF-like implosion conditions has been attained. Specifically, smaller cores, shorter burn phases, and higher neutron production rates are observed as preheat shielding is increased.

Performance vs Surface Roughness

Figure 8 shows primary neutron yield for undoped and doped capsules vs initial surface roughness. Between best surface finish (<0.03 μm rms) and 1 μm rms roughness, the yields of undoped capsules drop by a factor of only 1.5, while those of 1.3 at.% Ge-doped capsules drop by a factor of 6. This finding is qualitatively consistent with the transition from low- (GF ~10) to high-growth-factor (GF = 110) behavior expected with doping. Moreover, we observe a statistically significant factor-of-2 yield degradation between doped capsules with best surface finish and doped capsules with 0.1-μm rms roughness; from Fig. 1, the latter correspond closely to the 20% mix fraction growth that determines the NIF ignition threshold.

Figure 9 compares the averaged doped capsule yields vs surface finish with various simulation results. The lowest curve, which represents the atomic mix model with no saturation, severely overestimates the yield degradation for large initial surface roughnesses. The other curves represent the same model corrected for the different saturation behavior predicted for 3-D or 2-D multimode growth.[34] The atomic mix models are in fairly good agreement with data at the rough end. As discussed in the section on 3-D modeling advances, the factor of 3–4 yield discrepancy, which remains at the smooth capsule end can be largely accounted for by long wavelength capsule wall thickness variations. The larger yield degradation calculated for the 3-D saturation model is a consequence of the later onset of saturation[4] and of the higher terminal velocity of low-density 3-D fuel bubbles rising into the shell. The atomic mix model with the 2-D saturation prescription, although not strictly comparable with the 3-D nature of perturbation growth in the experiment, is included to show good agreement with 2-D finely zoned multimode simulations (shown as triangles).

These multimode simulations, which follow perturbation growth past saturation and do not need to combine modes into a 1-D mix description, were made possible by using only a few photon groups.[33] This method is

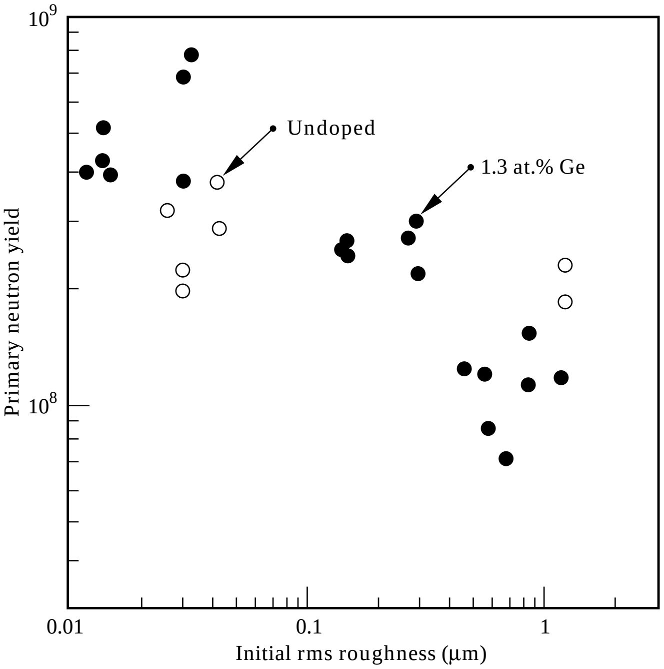

FIGURE 8. Measured primary neutron yields for 1.3 at.% Ge-doped (solid circles) and undoped (open circles) capsules vs initial rms surface roughness. (20-03-0995-2104pb01)

only applicable when diffusive radiation transport is used, speeding up computer simulations. The 3-D nature of the perturbations is accounted for by adjusting the 2-D surface power spectra so that each mode makes the same relative contribution to the total rms roughness as in three dimensions. As 2-D simulations are carried out on a 90° quadrant, power in odd modes is "aliased" into the adjacent even modes. At peak neutron emission time, the 2-D simulations show classic "bubble and spike" saturated RT growth for the dominant modes at the pusher–fuel interface for initial surface roughnesses greater than 0.1 µm. The effects of low-mode drive nonuniformities, which distort the pusher–fuel interface, were included in some 2-D multimode calculations. For example, the predicted extra yield degradation due to flux nonuniformities for a smooth, doped capsule is ~30%, as shown by the square in Fig. 9. More appropriate 3-D multimode simulations treating such flux asymmetries in their exact 3-D orientations are described under Recent Modeling Advances, below. In particular, the effects of synergism between growth of low-order surface perturbations and flux asymmetry–seeded perturbations are quantified there.

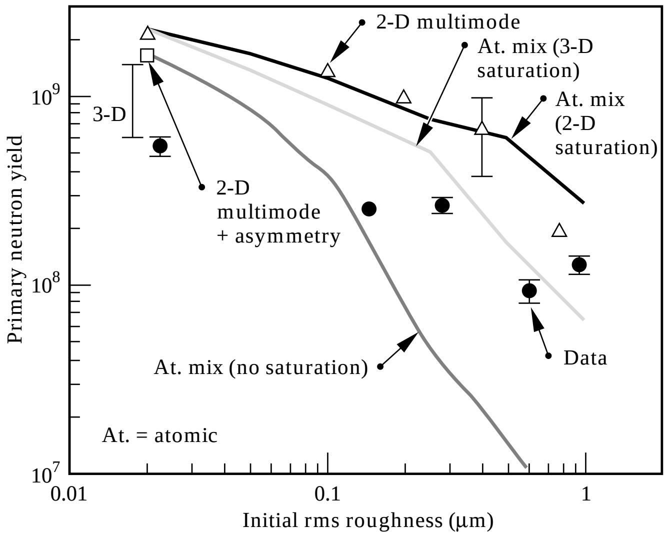

FIGURE 9. Measured and calculated primary neutron yields for 1.3 at.% Ge-doped capsules vs initial surface roughness. Solid circles are averaged data points from Fig. 8. Solid curves are predictions from the atomic mix model with no saturation, with a 2-D saturation, and with a 3-D saturation prescription. The square and the triangles are predictions from 2-D multimode simulations with and without flux nonuniformities. The vertical line at the upper left represents the range of yields calculated by the 3-D HYDRA code for a smooth capsule by varying the relative orientation between low-order capsule and radiation flux nonuniformities. (20-03-0995-2105pb01)

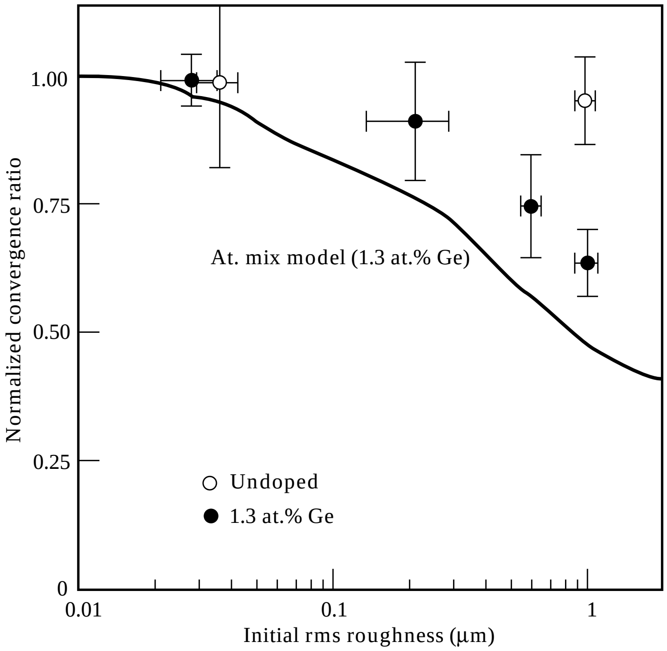

FIGURE 10. Relative capsule convergence (inferred from secondary neutron yields and spectra) vs initial surface roughness for undoped and 1.3 at.% Ge-doped capsules. The curve is a prediction for 1.3 at.% Ge doping, using the atomic mix model with 3-D saturation. Convergences are normalized to calculated convergence for smooth, doped capsules. (20-03-0995-2106pb01)

Figure 10 shows relative capsule convergences inferred from secondary-neutron yields and spectra from doped and undoped capsules vs initial surface roughness. The data points are averaged over capsules of similar roughness, and standard errors are shown. As expected, only the convergence of the high-growth, doped capsule drops significantly as capsule surface roughness is increased to 1 µm rms. The solid line is in fair agreement with the data. It represents post-processed predictions of the inferred convergence for 1.3 at.% Ge doping based on following the triton trajectory through both the pure fuel and the 1-D atomically mixed layer.

Figures 9 and 10 show that the primary and secondary gas yields are best suited to inferring large mix fractions. This is because the gas yield for nonigniting capsules is dominated by the hottest (central) region, which is farthest from the pusher–fuel interface and least affected by conduction cooling. By contrast, shell conditions can be most sensitive to small amounts of mix as penetrating spikes of shell material enter a region of steeply rising temperature.[6,13] For the lower-convergence HEP3 targets, moderate shell–gas mix was inferred from ratios of shell to gas dopant x-ray line emissivities.[6] Analogous measurements[23,30] attempted for HEP4 are sensitive to the significant x-ray reabsorption by the more converged and compressed shells. For example, for the Ar 3–1 lines, the shell optical depth at peak neutron production time is ~5.[13]

Deuterated-Shell Implosions

One technique for circumventing the problem of high shell x-ray opacity in inferring shell mix is to measure the neutron yields from capsules with deuterated shells.[35] Figure 11 shows a cross section of the capsule design. The only differences with respect to the usual capsule (Fig. 2) are a 75-atm H fill (to provide an inert fill with the same convergence as the 50-atm fill shown in Fig. 2) and a 4-µm-thick deuterated polystyrene inner shell. Peak growth factors are a factor of 2 higher, principally because the shell yield (which depends on thermal conduction) is delayed with respect to the fuel yield, allowing more time for perturbation growth. Small amounts of mix should now act to increase the yield by introducing D into the hotter central gas region. For example, the fusion rate at the ~1-keV temperature of interest and for an ion density n scales as n^2T^7, and hence as T^5 for a profile with constant pressure nT. For larger mix fractions, compression is reduced (see Fig. 10), reducing temperatures throughout the capsule. Therefore, after an initial rise in yield with increasing mix fraction, a drop in shell yield might be expected.

Figure 12 shows the observed dependence of shell primary yield on surface roughness. The implosion conditions were identical to those in the deuterated-fuel implosions except for a 7% lower drive designed to reduce ultra-hard x-ray contamination of the neutron diagnostics measuring the low yields. The yield remains nearly constant with increasing surface roughness up to 0.5 µm and finally falls for rougher surfaces. The standard atomic mix model with 3-D saturation, shown as the middle curve in Fig. 12, predicts only a slight increase in yield with surface roughness, in fair agreement with the data. The explanation for this behavior is that the shell yields are sensitive to an additional ingredient in the model that does not affect gas yields: an enhanced heat diffusivity term scaling as $\alpha L(dL/dt)$ over the 1-D mix layer of width L, where α is a heat diffusivity multiplier.[13] This extra heat flow is used to mimic the heat dilution that occurs as the surface area of a more realistic RT-modulated interface grows. The middle curve in Fig. 12 uses $\alpha = 1$, but the result changes little for α between 0.5 and 2. If α is set to 0, the top curve results, in significant disagreement with the data. The reduction in yield with enhanced heat diffusivity is a consequence of reducing temperature gradients in the mix region, thereby dropping peak temperatures in the innermost shell region, which dominates the yield. For NIF 1-D capsule designs, such a heat flux term is essential in the 1-D atomic mix model to correctly account for heat transfer from the inner hot DT gas to the outer cold DT pusher. The absence of H-like Ti shell emission in earlier experiments is also more consistent with a reduction in shell temperature gradients. By contrast, gas yields are factors of 5 less sensitive than shell yields to the heat diffusivity term; in the atomic mix predictions of gas yields shown in Fig. 9, we used $\alpha = 1$.

Figure 12 also shows predictions of 2-D multimode (l = 2, 4, 6,… , 48) and single-mode (l = 24) calculations, which are in good agreement with the data and with the atomic mix model, including enhanced heat diffusion. The simpler single-mode simulations assume that all the roughness is concentrated in a dominant mode. The predicted yields fall rapidly at about 0.4 µm rms roughness, for which the increased heat losses to the deuterated layer are insufficient to raise or even maintain the D temperature because of the reduced compressional

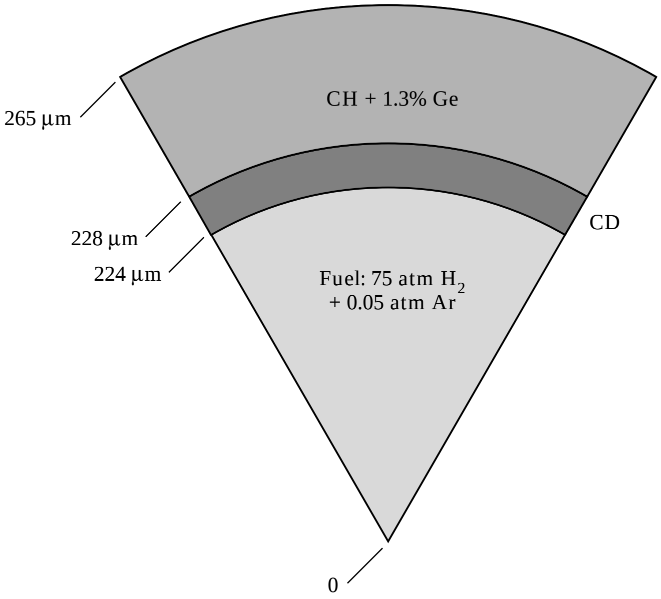

FIGURE 11. Cross section of a typical deuterated-shell capsule design. (20-03-0995-2107pb02)

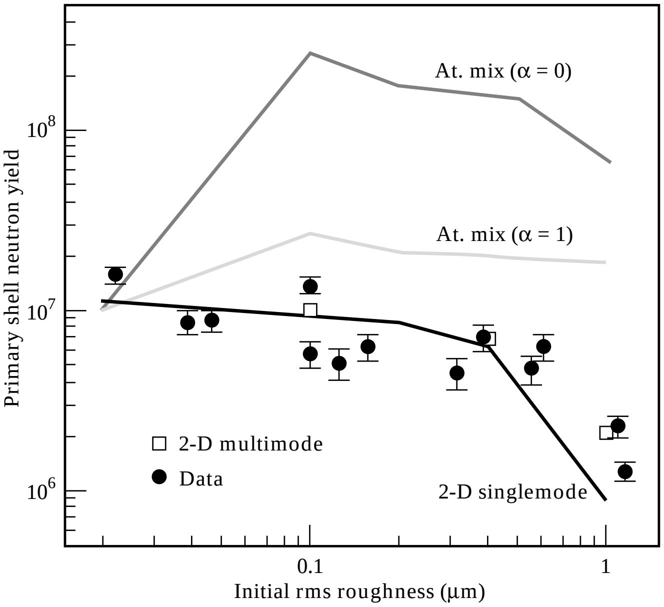

FIGURE 12. Measured and calculated primary yields for 1.3 at.% Ge-doped deuterated-shell capsules vs initial surface roughness. Solid circles are the data with experimental uncertainties. The top and middle curves are predictions from the atomic mix model without ($\alpha = 0$) and with ($\alpha = 1$) enhanced heat diffusion. The lower curve and squares are predictions from 2-D single-mode (l = 24) and multimode (l = 2, 4, 6,… , 48) simulations. (20-03-0995-2107pb01)

heating of the gas. For example, the peak compressional heating power in the implosion of a capsule with 1 µm rms roughness is only 72% of the unperturbed value. The simulations indicate shell breakup for capsules above 0.4 µm rms roughness.

Recent Modeling Advances

In current HEP4 work, we have advanced to 3-D modeling using the new HYDRA code.[33] Simulations in progress include modeling of both multimode and single-mode perturbation growth; additional distortion from radiation flux asymmetries can be included. The code uses multigroup radiation diffusion.

Figure 13 shows a snapshot of the ablation front and pusher–fuel interface for a typical single-mode growth simulation ($l = 18$) of a 0.25-µm rms perturbation. The interfaces shown represent an isodensity surface at 17.2 g/cm^3, 40 ps before peak neutron production time. The white contour lines show the 90° × 36° repeating sector used in the simulation. The 92 pits on the outside surface (modeled as hyperGaussians) have fed through to form bubbles of fuel rising into the shell and parabolic ridges of shell material penetrating the fuel. A Kelvin–Helmholz instability at the fuel–pusher interface causes significant roll-up in the bubble tips. The calculated yield was 82% of the yield for a perfectly smooth capsule surface.

Recently, the measured lowest-order capsule imperfections have been added to the input of a 3-D multimode simulation, which included radiation flux asymmetries. In particular, the importance of a worst-case 5-µm variation in capsule shell thickness from pole to equator has been studied. By aligning the capsule so that the thinnest part of the shell faces the hohlraum midplane, where a combination of P_2 and $m = 5$ radiation flux asymmetries already act coherently, 3-D HYDRA simulations predict a 60% drop in yield, from 1.44×10^9 to 6×10^8 (see Fig. 9). The yield drops sharply because the thinner sections of the shell converge faster and allow spikes of shell material from RT growth of $m = 5$ seeded perturbations to meet at peak neutron emission time. Hence, the scatter in the smooth capsule yields may be due to the arbitrary capsule-to-hohlraum orientation inherent during target assembly and the variable amplitude of lowest-order fluctuations in capsule shell thickness.

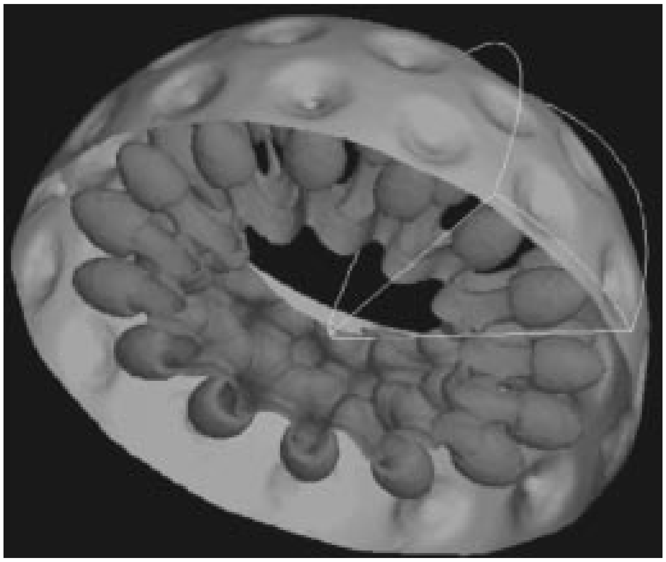

FIGURE 13. Three-dimensional simulation of isodensity (17.2 g/cm^3) surface contour of imploded capsule, 40 ps before peak neutron emission time. Outside surface (70 µm diam) shows ablation front growth. Initial perturbation was a 0.25-µm rms single-mode pattern ($l = 18$) created by 92 pits on 1.3 at.% Ge-doped capsules. White contour lines define the 90° × 36° repeating sector used in the simulation. (08-00-0695-1495pb01)

Conclusion

Low-entropy Nova implosions using x-ray preheat shielded, doped plastic capsules with reproducible, well-characterized pre-roughened surface finishes have demonstrated large hydrodynamic instability growth similar to that expected in ignition-scale targets. The expected transition to lower entropy and higher instability growth, and hence to ignition-scalable behavior, was experimentally demonstrated by comparing the performance of doped and undoped capsules inferred from x-ray and neutron measurements. To avoid difficulties with high shell x-ray opacities, pusher–fuel mix was inferred from neutron yields rather than from the dopant x-ray line ratios described in HEP3. The large scatter in the yields of the smoothest capsules may be related to the arbitrary orientation of low-order capsule-shell-thickness nonuniformities with respect to radiation-seeded asymmetries, which could lead to large differences in imploded capsule shape. Average neutron yields for the smoothest capsules remain lower than expected for both undoped and doped capsules, although 3-D calculations which include the low order capsule, wall thickness variations are expected to significantly reduce this discrepancy. Neutron yields from roughened capsules suggest that there is similar or less growth than predicted by models including growth saturation, thereby validating current capsule surface finish requirements for ignition designs. Yields from complementary deuterated-shell experiments agreed with the models and clearly show that enhanced heat diffusion must be included in the traditional atomic mix model.

Acknowledgments

We thank B. A. Remington, S. V. Weber, J. D. Kilkenny, and J. D. Lindl for their useful input. The authors are also indebted to the LLNL (and LANL) staff for providing high-quality targets, diagnostic maintenance, and laser shots.

Notes and References

1. J. H. Nuckolls, L. Wood, A. Thiessen, and G. B. Zimmerman, *Nature* **239**, 139 (1972).
2. J. D. Lindl, R. L. McCrory, and E. M. Campbell, *Phys. Today* **45**, 32 (1992).
3. J. Meyer-ter-Vehn, *Nucl. Fusion* **22**, 561 (1982).
4. S. W. Haan, *Phys. Fluids B* **3**, 2349 (1991); S. W. Haan, *Phys. Rev. A* **39**, 5812 (1989).
5. J. D. Kilkenny, S. G. Glendinning, S. W. Haan, B. A. Hammel, et al., *Phys. Plasmas* **1**, 1379 (1994).
6. T. R. Dittrich, B. A. Hammel, C. J. Keane, R. McEachern, et al., *Phys. Rev. Lett.* **73**, 2324 (1994).
7. J. D. Lindl and W. C. Mead, *Phys. Rev. Lett.* **34**, 1273 (1975); S. E. Bodner, *Phys. Rev. Lett.* **33**, (1974); H. Sakagami and K. Nishihara, *Phys. Fluids B* **2**, 2715 (1990).
8. R. D. Richtmyer, *Commun. Pure Appl. Math.* **13**, 297 (1960); E. E. Meshkov, *Izv. Akad. Nauk. SSSR, Mekh. Zhidk. Gaz.* **5**, 151 (1969) (NASA TTF-13-074, 1970).
9. Lord Rayleigh, *Scientific Papers* (Cambridge Univ. Press, Cambridge, 1900), Vol. II, p. 200.
10. H. Takabe, K. Mima, L. Montierth, and R. L. Morse, Phys. Fluids 28 (1985); D. H. Munro, *Phys. Rev. A* **38**, 1433 91988); M. Tabak, D. H. Munro, and J. D. Lindl, *Phys. Fluids B* **2**, 1007 (1990).
11.
12. J. H. Gardner and S. E. Bodner, *Phys. Rev. Lett.* **47**, 1137 (1981); B. Yaakobi, J. Delettrez, L. M. Goldman, R. L. McCrory, et al., *Opt. Commun.* **41**, 355 (1982); H. Nishimura, T. Kiso, H. Shiraga, T. Endo, et al., *Phys. Plasmas* **2**, 1 (1995).
13. C. J. Keane, R. C. Cook, T. R. Dittrich, B. A. Hammel, et al., *Rev. Sci. Instrum.* **66**, 689 (1995); C. J. Keane, G. W. Pollak, R. C. Cook, T. R. Dittrich, et al., *J. Quant. Spectrosc. Radiat. Transfer* **54**, 207 (1995).
14. R. Pakula and R. Sigel, *Phys. Fluids* **28**, 232 (1985); M. Murakami and J. Meyer–ter–Vehn, *Nucl. Fusion* **31**, 1315 (1991); R. L Kauffman, L. J. Suter, C. B. Darrow, J. D. Kilkenny, et al., *Phys. Rev. Lett.* **73**, 2320 (1994).
15. S. V. Weber, B. A. Remington, S. W. Haan, B. G. Wilson, and J. K. Nash, *Phys. Plasmas* **1**, 3652 (1994).
16. B. A. Remington, S. W. Haan, S. G. Glendinning, J. D. Kilkenny, et al., *Phys. Rev. Lett.* **67**, 3259 (1991); B. A. Remington, S. V. Weber, S. W. Haan, J. D. Kilkenny, et al., *Phys. Fluids B* **5**, 2589 (1993).
17. S. W. Haan et al., *Phys. Plasmas* **2**, 2480 (1995).
18. R. Cook, G. E. Overturf, S. R. Buckley, and R. McEachern, *J. Vac. Sci. Technol. A* **12**, 1275 (1994).
19. R. J. Wallace, R. L. McEachern, and W. W. Wilcox, *ICF Quarterly Report* **4**(3), 79, Lawrence Livermore National Laboratory, Livermore, CA, UCRL-LR-105821-94-3 (1994).
20. R. L. McEachern, C. Moore, G. E. Overturf, III, S. R. Buckley, and R. Cook, *ICF Quarterly Report* **4**(1), 25 Lawrence Livermore National Laboratory, Livermore, CA, UCRL-LR-105821-94-1 (1994).
21. S. M. Pollaine, S. P. Hatchett, and S. H. Langer, *ICF Quarterly Report* **4**(3), 87, Lawrence Livermore National Laboratory, Livermore, CA, UCRL-LR-105820-94-3 (1994).
22. C. W. Laumann, J. A. Caird, J. E. Murray, R. E. McEachern, et al., *ICF Quarterly Report* **4**(1), 1–30, Lawrence Livermore National Laboratory, Livermore, CA, UCRL-LR-105820-94-1 (1994).
23. E. M. Campbell, *Laser Part. Beams* **9**, 209 (1991); B. A. Hammel, C. J. Keane, T. R. Dittrich, D. R. Kania, et al., *J. Quant. Spectrosc. Radiat. Transfer* **51**, 113 (1994).
24. H. N. Kornblum, R. L. Kauffman, and J. A. Smith, *Rev. Sci. Instrum.* **57**, 2179 (1986).
25. M. D. Cable, S. P. Hatchett, J. A. Caird, J. D. Kilkenny, et al., *Phys. Rev. Lett.* **73**, 2316 (1994).
26. R. L. Kauffman, H. N. Kornblum, D. W. Phillion, C. B. Darrow, et al., *Rev. Sci. Instrum.* **66**, 678 (1995).
27. M. D. Cable and S. P. Hatchett, *J. Appl. Phys.* **62**, 2223 (1987).
28. R. A. Lerche, D. W. Phillion, and G. L. Tietbohl, *Rev. Sci. Instrum.* **66**, 933 (1995).
29. J. D. Kilkenny, *Laser and Part. Beams* **9**, 49 (1991).
30. O. L. Landen, C. J. Keane, B. A. Hammel, M. D. Cable, et al., *J. Quant. Spectrosc. Radiat. Transfer* **54**, 245 (1995).
31. C. J. Keane, B. A. Hammel, D. R. Kania, J. D. Kilkenny, et al., *Phys. Fluids B* **5**, 3328 (1993); C. J. Keane, B. A. Hammel, A. L. Osterheld, and D. R. Kania, *Phys. Rev. Lett.* **72**, 3029 (1994).
32. G. B. Zimmerman and W. L. Kruer, *Comm. Plasma Phys. Controlled Fusion* **11**, 51 (1975).
33. M. M. Marinak, B. A. Remington, S. V. Weber, R. E. Tipton, et al., “Three-Dimensional Single Mode Rayleigh-Taylor Experiments on Nova,” Lawrence Livermore National Laboratory, Livermore, CA, UCRL-JC-120191 (1995); submitted to *Phys. Rev. Lett.*; M. M. Marinak, R. E. Tipton, B. A. Remington, S. W. Haan, and S. V. Weber, *ICF Quarterly Report* **5**(3), p. 168, Lawrence Livermore National Laboratory, Livermore, CA, UCRL-LR-105821-95-3 (1995).
34. C. J. Keane, O. L. Landen, B. A. Hammel, P. Amendt, et al., “Observation of Large-Growth Factor Behavior in Indirectly Driven Spherical Implosions,” Lawrence Livermore National Laboratory, Livermore, CA, UCRL-JC-123022 ABS (1995).
35. R. E. Chrien, N. M. Hoffman, and J. D. Colvin, “Fusion Neutrons from the Gas-Pusher Interface in Deuterated-Shell ICF Implosions,” Los Alamos National Laboratory, Los Alamos, NM, LA-UR-95-2307 (1995).